nature catalysis

SUPPLEMENTARY INFORMATION

https://doi.org/10.1038/s41929-018-0148-8

In the format provided by the authors and unedited.

Solar energy-driven lignin-first approach to full utilization of lignocellulosic biomass under mild conditions

Xuejiao Wu[1,2], Xueting Fan[1,2], Shunji Xie[1,2], Jinchi Lin[1], Jun Cheng[1]*, Qinghong Zhang[1]*, Liangyi Chen[1] and Ye Wang[1]*

[1]State Key Laboratory of Physical Chemistry of Solid Surfaces, Collaborative Innovation Center of Chemistry for Energy Materials, National Engineering Laboratory for Green Chemical Productions of Alcohols, Ethers and Esters, College of Chemistry and Chemical Engineering, Xiamen University, Xiamen, China. [2]These authors contributed equally to this work: Xuejiao Wu, Xueting Fan, Shunji Xie *e-mail: chengjun@xmu.edu.cn; zhangqh@xmu.edu.cn; wangye@xmu.edu.cnTable 1 | **Products from photocatalytic conversions of lignin models and birch woodmeal**

Solar energy-driven lignin-first approach to full utilization of lignocellulosic biomass under mild conditions

Xuejiao Wu[†], Xueting Fan[†], Shunji Xie[†], Jinchi Lin, Jun Cheng*, Qinghong Zhang*, Liangyi Chen and Ye Wang*

State Key Laboratory of Physical Chemistry of Solid Surfaces, Collaborative Innovation Center of Chemistry for Energy Materials, National Engineering Laboratory for Green Chemical Productions of Alcohols, Ethers and Esters, College of Chemistry and Chemical Engineering, Xiamen University, Xiamen 361005, China.

*Correspondence and requests for materials should be addressed to J.C. (chengjun@xmu.edu.cn), Q.Z. (zhangqh@xmu.edu.cn) or Y.W. (wangye@xmu.edu.cn).

[†]These authors contributed equally to this work.

Table of content

Supplementary Table 4 | Integrated results of monomers and linkages in birch woodmeal based on the 2D HSQC NMR spectra

Supplementary Table 5 | Lists of monomeric products from photocatalytic conversion of native lignin in birch woodmeal

Supplementary Table 6 | Photocatalytic conversion of native lignin in birch woodmeal using different catalysts as well as photocatalytic conversion of PP-ol using CdS-MPE

Supplementary Table 7 | Compositions of birch woodmeal before and after photocatalytic conversion of native lignin

Supplementary Table 8 | Retention time and effective carbon number (ECN) of major products

Supplementary Table 9 | Calculated dehydrogenation potential (in V) of PP-ol in vacuum and on CdS surfaces by using the PBE and the HSE06 functionals

Supplementary References

Supplementary Methods

General considerations

All chemicals available commercially were purchased and used as received, unless otherwise noted. Birch sample was obtained from local shops and was ball-milled to pass through a 1-mm screen. Before conducting the photocatalytic conversion, the sample was purified with ethanol/benzene mixture (4:1 v/v) for 3 h, dried at 105 ºC overnight and placed in a desiccator for 2 h.

Two-dimensional heteronuclear single quantum coherence NMR (2D HSQC NMR) spectroscopic measurements were performed with a Bruker Avance III 850 MHz spectrometer equipped with a 5 mm TXI $^{1}H/^{13}C/^{15}N$ cryo-probe. The central DMSO solvent peak was used as an internal reference. A high-performance liquid chromatograph (HPLC, Shimadzu LC-20AD) equipped with a refractive index detector (RID-10A), a diode array detector (SPD-M20A) and an InertSustain C18 column was used to quantify the products obtained from the conversion of lignin model compounds. The mobile phase was a mixture of CH_3CN and H_2O with a ratio of 6:4 at 35 ºC. Shodex-Sugar column was used to quantify monosaccharide and the mobile phase was a 0.05M H_2SO_4 solution at 50 ºC. The products obtained from the conversion of native lignin in lignocellulose were quantified by an Agilent 7890A series gas chromatograph (GC) equipped with a HP5-MS capillary column and a flame ionization detector (FID). The products were identified or confirmed by a Shimadzu GC2010 GC−MS equipped with an Rxi-5ms capillary column and a Shimadzu QP2010 mass-spectrometer detector. Authentic samples of major products, including 1-(3,5-dimethoxy-4-hydroxyphenyl)-1-propanone, 1-(4-hydroxy-3-methoxyphenyl)propan-1-one, 4-hydroxypropiophenone, (4-

hydroxy-3,5-dimethoxy-phenyl)-acetone and 4-hydroxy-3-methoxyacetophenone were used to reconfirm the assignment.

The catalyst was characterized by powder X-ray diffraction (XRD), transmission electron microscopy (TEM), diffuse reflectance ultraviolet-visible (UV-vis) spectroscopy, UV-vis absorption spectroscopy, inductively coupled plasma mass spectrometry (ICP-MS) and photoelectrochemical measurements. XRD patterns were recorded on a Panalytical X'pert Pro diffractometer using Cu Kα radiation (40 kV, 30 mA). TEM and high-resolution TEM (HRTEM) measurements were performed on a Tecnai F20 electron microscope (Phillips Analytical) operated at an acceleration voltage of 200 kV. UV-vis spectroscopy measurements were carried out on a Varian-Cary 5000 spectrophotometer. Photoelectrochemical measurements were performed with CHI 760E using a standard three electrode cell with a working electrode, a Pt plate as the counter electrode and an SCE electrode as the reference electrode. The electrodes of quantum dot films (1.0×1.0 cm^2) were prepared by drop-coating CdS QDs dispersed solution on F/SnO_2 substrates and drying in the dark overnight. The films were immersed in an aqueous electrolyte solution containing 1.0 M KCl and 0.1 M Na_2SO_3, and the electrochemical scans were conducted with a scan rate of 10 mV s^{-1}. ICP-MS measurements were performed using an Agilent ICP-MS 4500 instrument. The detection limit of Agilent ICP-MS 4500 for cadmium is 0.02 ppb. After photocatalytic reactions and removal of catalyst, the reaction solution was evaporated to remove the solvent. Then, the sample was dissolved in 25 mL 5 vol.% hydrochloric acid aqueous solution for ICP-MS measurements.

Synthesis of CdS nanoparticles and CdS quantum dots with different sizes

CdS nanoparticles (NPs) were synthesized by a hydrothermal method reported previously[1].

3.5 mmol $Cd(NO_3)_2$ was added into 40 mL deionised water, and 4.0 mmol Na_2S was dissolved in 20 mL deionised water. The latter solution was added dropwise into the former one under continuous stirring. After further stirred at room temperature for 0.5 h, the mixture was transferred into a Teflon-lined stainless steel autoclave and was subject to hydrothermal treatment at 180 ºC for 12 h. After the hydrothermal treatment, the solid was collected by centrifugation and washing with deionised water for several times and then drying at 80 ºC.

CdS quantum dots (QDs) were synthesized by the typical hot-injection method[2]. The size of CdS QDs was regulated by adjusting the concentration of organic ligand and the temperature. In brief, a mixture of 1-octadecene (ODE) (36 mL), CdO (3 mmol) and oleic acid was heated to 280 ºC under argon atmosphere. The uses of oleic acid with volumes of 3, 5, 10 and 18 mL could result in CdS QDs with sizes of 3.8, 4.4, 5.0 and 6.1 nm, respectively. A solution of sulphur (1.5 mmol) in ODE was swiftly injected into this hot solution and the mixture was cooled down to a specified temperature (220 ºC for 3.8 and 4.4 nm QDs, 240 ºC for 5.0 and 6.1 nm QDs). The solution was maintained at that temperature for 1 h to allow the growth of CdS QDs. After cooled down to room temperature, the synthesized CdS QDs were purified with acetone and ethanol. The purified QDs were dissolved in chloroform.

Ligand exchange

Ligand exchange with 3-mercaptopropionic acid (MPA) or 1-mercaptopropane (MPE) was carried out according to a literature procedure[3]. MPA or MPE (1 mL) was dispersed in 1:1 chloroform/methanol (20 mL) and the pH value was adjusted to about 11 with tetramethylammonium hydroxide (TMAOH). The QDs (30 mg) synthesized by above procedure were added to this mixture and stirred at 55 ºC in the dark overnight. The QDs were

aggregated and washed with excess amounts of acetone. In some cases, the ligand was removed by addition of moderate amounts of HCl (2 M). After washing, the CdS-MPA can be re-dispersed in water. The CdS-MPA was typically used for photocatalytic conversion of lignin in birch woodmeal.

Procedure for isolation of the major product

Birch woodmeal of 1.2 g was divided into four batches (4×300 mg) and each was loaded into a 50 mL quartz reactor. The reaction conditions were basically the same with those for the regular-scale (100 mg birch woodmeal) conversion of native lignin except for using a reaction time of 16 h. The product mixtures were combined and concentrated to about 0.5 mL, and injected into preparative HPLC equipped with C18 column. The preparative HPLC was operated with a gradient mobile phase system consisting of H_2O and CH_3CN at a flow rate of 4 mL min^{-1}. The weight of the isolated 1-(3,5-dimethoxy-4-hydroxyphenyl)-1-propanone, the major product, was 24 mg, corresponding to a yield of 10.6 wt%.

Gel-NMR (2D HSQC) experiment for birch woodmeal

NMR experiments for the birch woodmeal were performed using the method reported previously[4]. The spectra were acquired on a Bruker Avance III 850 MHz spectrometer equipped with a 5 mm TXI 1H/13C/15N cryo-probe. Birch woodmeal (50 mg) was transferred directly into the NMR tube. Then, 0.5 mL dimethyl sulfoxide (DMSO)-d_6/pyridine-d_5 (4:1) was introduced into the NMR tube, and the mixture was sonicated for 2 h to form a homogeneous gel. The central DMSO solvent peak was used as internal reference (δC 39.5, δH 2.49 ppm). The standard Bruker pulse sequence 'hsqcetgpsp.2.2' was used for ^{1}H and ^{13}C-HSQC experiments. 2048 data points were acquired in F2 dimension (acquisition time 142 ms) with

a 12 ppm spectral width centred on 5.5 ppm. 128 increments were acquired in the F1 dimension (acquisition time 4.9 ms) with a spectral width of 120 ppm centred on 100 ppm. The total experimental time was about 2 h.

Compositional analyses of birch woodmeal and carbohydrate residue after photocatalytic reaction

The analyses of compositions of birch and the solid residue after photocatalytic reaction were performed by a method reported previously[5,6]. The analytical procedure is displayed in Supplementary Fig. 7. Both samples were analysed in triplicate. The results are presented in Supplementary Table 7.

Models of CdS surfaces and the computational setup

The CdS(110) surface was modelled by periodic slabs with lateral dimensions of a 3 × 4 surface cell. A six-layer slab was used to ensure the convergence of the thickness. The slab was separated with its images by a vacuum region of 40 Å, leading to an orthorhombic super-cell of 17.496 × 16.495 × 55.310 $Å^3$. The periodic boundary conditions (PBC) were applied for the XY directions with the periodicity in the Z direction removed to eliminate the possible dipole interactions between the slabs with its images. The bottom two layers were fixed during geometry optimization.

Density functional theory (DFT) calculations were carried out using the freely available program package CP2K/Quickstep[7]. The DFT implementation in Quickstep is based on a hybrid Gaussian plane wave (GPW) scheme. Orbitals are described by an atom-centred Gaussian-type basis set, while an auxiliary plane wave basis is used to re-expand the electron density[8]. The wave function optimization was performed using an efficient orbital

transformation minimizer, which avoids the traditional matrix diagonalization method and gives optimal convergence control[9]. Analytic Goedecker-Teter-Hutter (GTH) pseudopotentials[10] were employed to represent the core electrons. The basis sets for the valence electrons of Cd and S ($4d^{10}5s^2$ for Cd and $3s^2$ $3p^4$ for S) consist of short-ranged (less diffuse) double-ζ basis functions with one set of polarization functions (DZVP) and basis sets for the valence electrons of O, H and C ($2s^22p^4$ for O, $1s^1$ for H and $2s^22p^2$ for C) consist of tripe-ζ basis functions with one set of polarization functions (TZVP)[11]. The plane wave basis for the electron density expansion was cut off at 400 Ry. All the simulations only used the Γ point of the supercell for expansion of the orbitals considering the large size of the cell. The convergence criterion for wave function optimization was set by a maximum electronic gradient of 3×10^{-7} a.u. and an energy difference tolerance between self-consistent field (SCF) cycles of 10^{-13} a.u. The gradient-corrected Perdew-Burke-Ernzerhof (GGA-PBE) functional[12] and hybrid HSE06[13,14] were used with the Grimme's dispersion correction[15]. Hybrid functional calculations applied an auxiliary density matrix method (ADMM)[16-20]. In this method, the density matrix is re-expanded in a small auxiliary basis set leading to massive speed-up of the calculation of Hartree Fock exchange (HFX).

Calculation of oxidative dehydrogenation of PP-ol

The oxidative dehydrogenation (ODH) reaction can be written as $XH \rightarrow X^* + \frac{1}{2}H_2\ (g)$. The hydrogen atom removed from XH is transformed to (half) a hydrogen molecule in gas phase. Following the formulation in the previous publications[16,20], the ODH free energy denoted by ΔG^{o}_{dh} can be expressed as:

$$\Delta G^{o}_{dh} = (E_{XH} - E_{X}) - \Delta_f G_{H^+} + k_B T \ln\left[c^o \Lambda^3_{H^+}\right] - \Delta_{zp} E_{H(OH_2)^+} \qquad (1)$$

in which E_{XH} and E_X are the total energies of PP-ol and the corresponding dehydrogenated states, and the total energy difference is used to estimate the free energy change assuming the entropic contributions are small (see previous work for validation[21]). The last three terms on the right hand side of the equation correspond to the formation free energy of a gas-phase proton (15.81 eV), the correction for the translation entropy of a proton at the standard concentration (-0.19 eV), and the zero-point energy of the X-H bond (0.35), respectively[20]. This ODH free energy as defined can be readily converted into a potential scale with respect to the standard hydrogen electrode (SHE) by using $\Delta G^{o}_{dh} = eU^{o}_{dh}$. They can be directly compared against the valence band position of CdS as shown in Fig. 5b in the main text.

We calculated the adsorption of PP-ol on the CdS(110) surface. A few structures were obtained after geometry optimization with similar adsorption energies, indicating that the molecule has a rather flat energy landscape on the surface. The three dehydrogenation radical states after C_α−H, C_β−H and O−H cleavage were also calculated. Care was taken to ensure that the correct spin states were obtained. The structures of the adsorbed molecules are shown in Supplementary Fig. 9, and the spin density of the radicals is visualized by green isosurfaces.

Substituting the total energies of these states into Supplementary Equation 1, we calculated the ODH energies for C_α−H, C_β−H and O−H cleavage, as listed in Supplementary Table 9. PBE and hybrid HSE06 functionals were used for these calculations, and both gave similar structures and energies. As can be seen from Supplementary Table 9, the dehydrogenation energies on the CdS surface are very close to those in vacuum, indicating that adsorption on CdS does not play an important role in weakening the C−H and O−H bonds in PP-ol. Most importantly, the breaking of C_α−H bond has the least positive potential, and thus is the most

likely to occur when PP-ol is oxidized by holes at the valence band of CdS.

Calculation of bond dissociation energies and redox potentials

The bond dissociation energies (BDE) of the C_β–O bonds in PP-ol, PP-one and the C_α radical intermediate were calculated, as well as the BDE of the bonds adjacent to C_α in the C_α radical intermediate, as shown in Supplementary Fig. 10. As shown in the calculations above, the adsorption on CdS surface plays little role in the energetics, and therefore these calculations were performed without the surface using the GAUSSIAN 09 program package[22]. The B3LYP functional[23,24,25] and the aug-cc-pVDZ[26] basis sets were employed. The CPCM(UAHF)[27,28] implicit solvation model was used to account for the solvation effect with the dielectric constant chosen as 55.7[29] to be consistent with the experimental condition (solvent CH_3CN used). Test calculations on other solvent parameters indicate little impact on solvation energies. Note that we also calculated the BDE without the solvation model and with the PCM model but with a different dielectric constant, and found there were little changes in the numbers, as solvation effects are small for neutral molecules and radicals. Optimized structures were checked by calculating vibrational frequencies to ensure the absence of imaginary frequencies.

The redox potential of the reductive bond dissociation of the C_α radical intermediate and the reduction potential of the phenoxy radical were calculated to compare against the conduction band minimum of CdS. They were also calculated using the GAUSSIAN 09 program package[22]. The B3LYP functional[23,24,25] and the aug-cc-pVDZ basis sets[26] were used, and the CPCM(UAHF) solvation model[27,28] was applied. These setups were well tested in the group to reproduce the redox potentials and pKa's of many molecules.

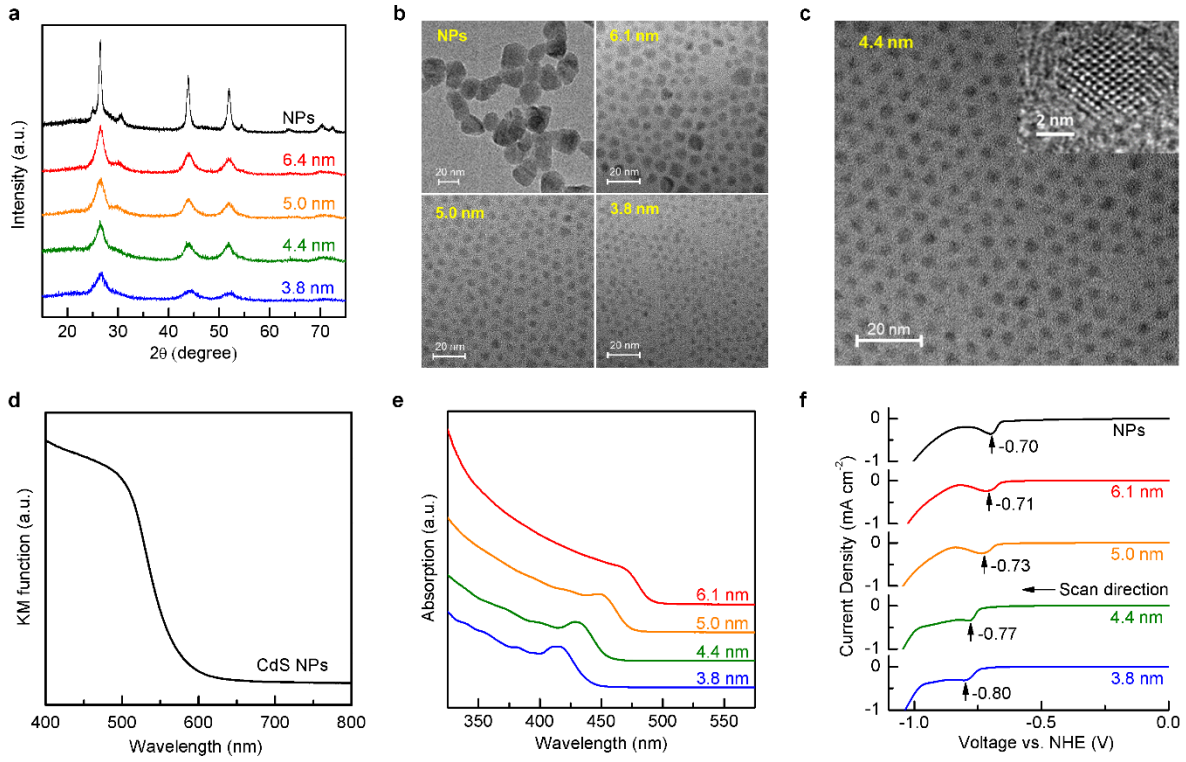

Supplementary Figure 1 | Basic characterizations of CdS NPs and CdS QDs of different sizes. **a,** XRD patterns. **b,** TEM micrographs of CdS NPs and CdS QDs with sizes of 6.1 nm, 5.0 nm and 3.8 nm. **c,** TEM and HRTEM (inset) micrographs of CdS QDs with a size of 4.4 nm. The result shows that CdS colloidal nanocrystals are single crystals with cubic zinc blende structure. **d,** Diffuse reflectance UV-vis spectrum of CdS NPs. The bandgap energy of CdS NPs is 2.35 eV. **e,** UV-vis absorption spectra of CdS QDs of different sizes. The result shows that bandgap energy of CdS QDs increases from 2.53 to 2.84 eV when their sizes decrease from 6.1 nm to 3.8 nm. **f,** Electrochemical scans of CdS NPs and CdS QDs of different sizes. The reduction peak marked with an arrow can be ascribed to the reduction of Cd^{2+}, which is equivalent to the E_{CB} of CdS.

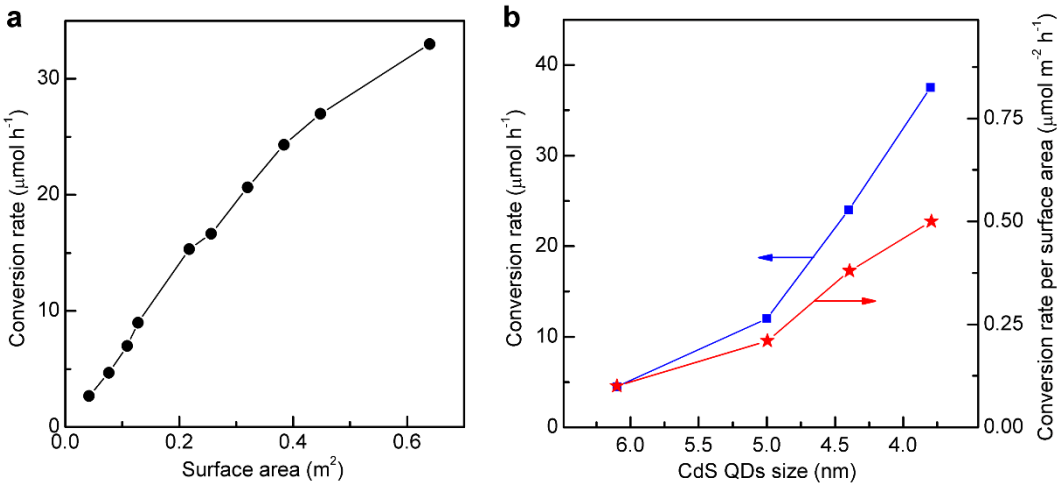

Supplementary Figure 2 | Conversion rates of PP-ol catalysed by CdS QDs. **a,** Change of conversion rate with surface area by changing catalyst amount. Reaction conditions: catalyst, CdS QD−4.4 nm; reactant, PP-ol, 0.1 mmol (20 mg); solvent, CH_3CN, 5.0 mL; atmosphere, N_2; light source, Xe lamp (λ = 420-780 nm), 300 W; irradiation time, 3 h. **b,** Conversion rate and conversion rate per surface area for CdS QDs with different sizes using LED-light irradiation. Reaction conditions: catalyst, CdS QDs, 10 mg; reactant, PP-ol, 0.1 mmol (20 mg); solvent, CH_3CN, 5.0 mL; atmosphere, N_2; light source, LED light (λ = 395 nm); irradiation time, 2 h. The BET surface areas for CdS QDs with sizes of 6.1, 5.0, 4.4 and 3.8 nm were 43, 57, 64 and 75 $m^2\ g^{-1}$, respectively.

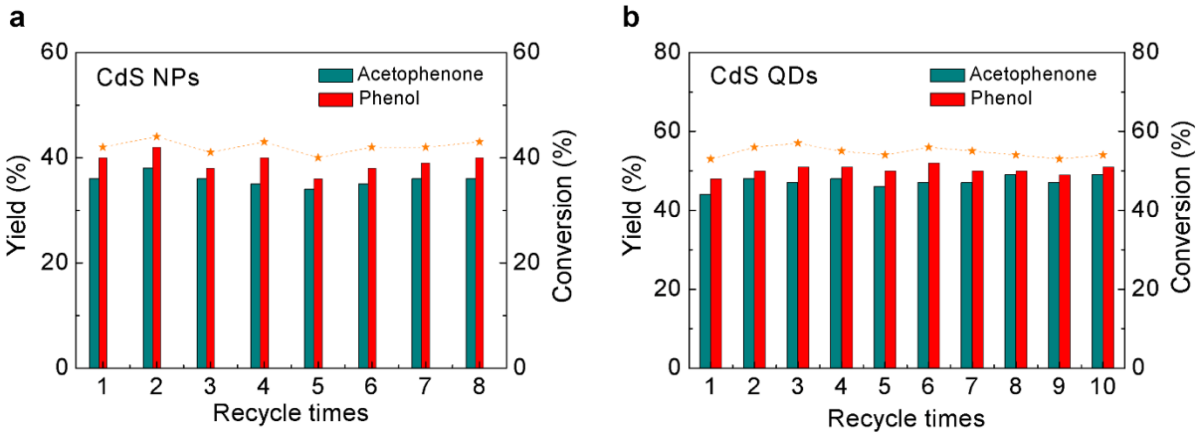

Supplementary Figure 3 | Changes of catalytic performances during recycling uses. **a,** CdS NPs for 8 recycles. **b,** CdS QD−4.4 nm for 10 recycles. Reaction conditions: catalyst, 10 mg; reactant (PP-ol), 40 mg (0.2 mmol); solvent, CH_3CN, 5.0 cm^3; atmosphere, N_2; light source, Xe lamp (λ = 420-780 nm), 300 W; irradiation time, 12 h for CdS NPs and 3 h for CdS QDs.

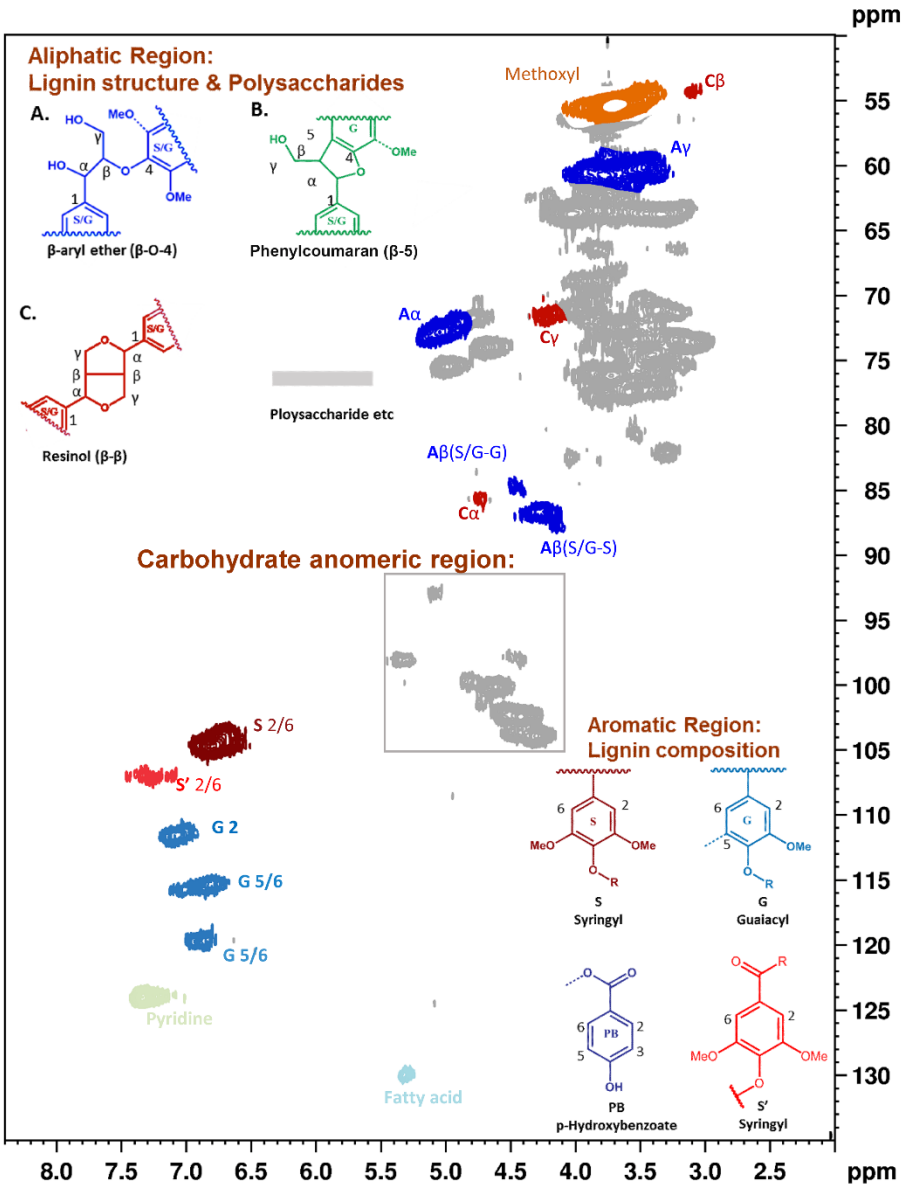

Supplementary Figure 4 | 2D HSQC NMR spectrum of birch woodmeal. Aα, Aβ and Aγ denote the C−H in α, β and γ carbons of β-O-4 linkages. Bα, Bβ and Bγ denote the C−H in α, β and γ carbons of phenylcoumaran units. Cα, Cβ and Cγ denote the C−H in α, β and γ carbons of resinol units.

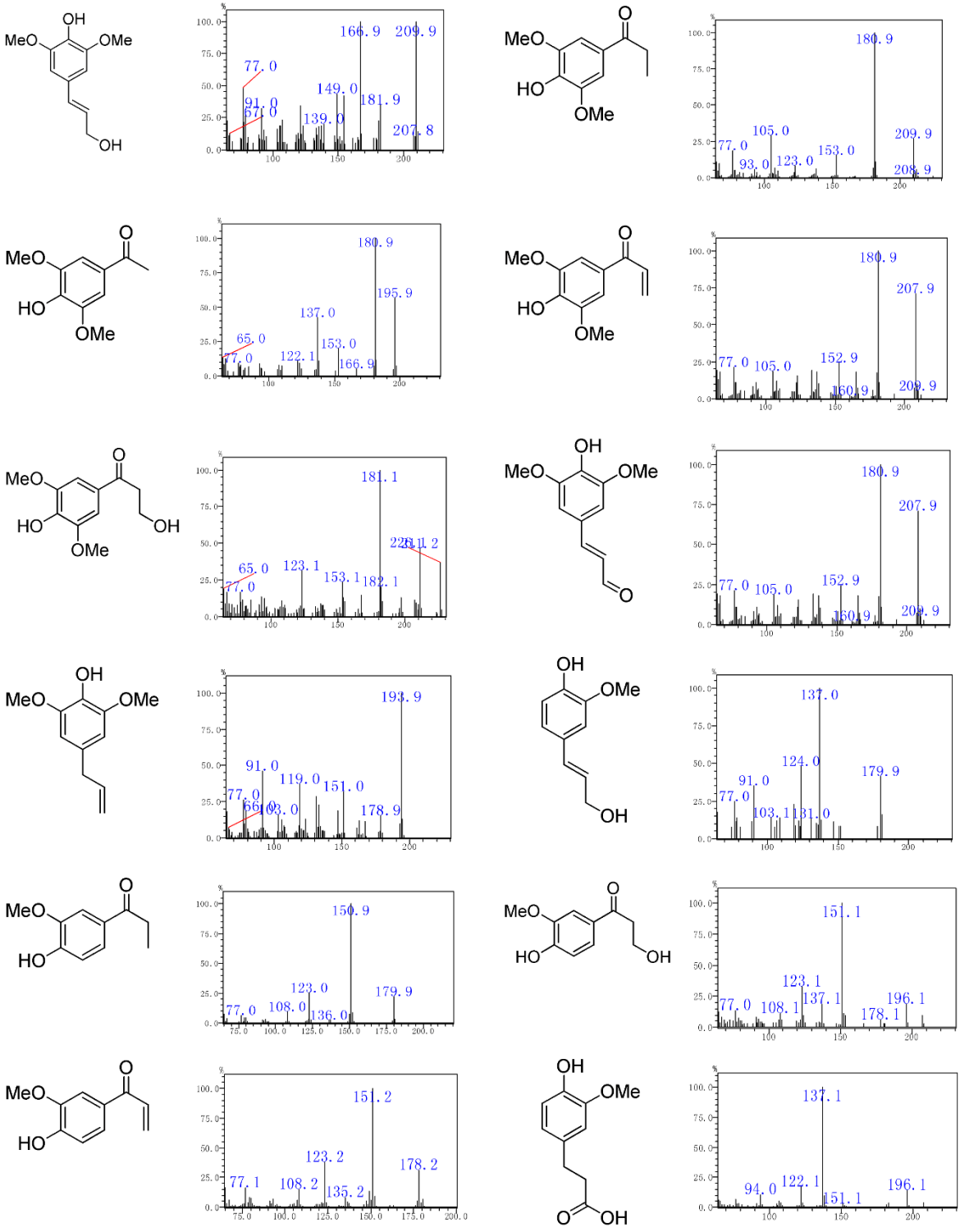

Supplementary Figure 5 | Mass spectra of products from the photocatalytic conversion of native lignin in birch woodmeal.

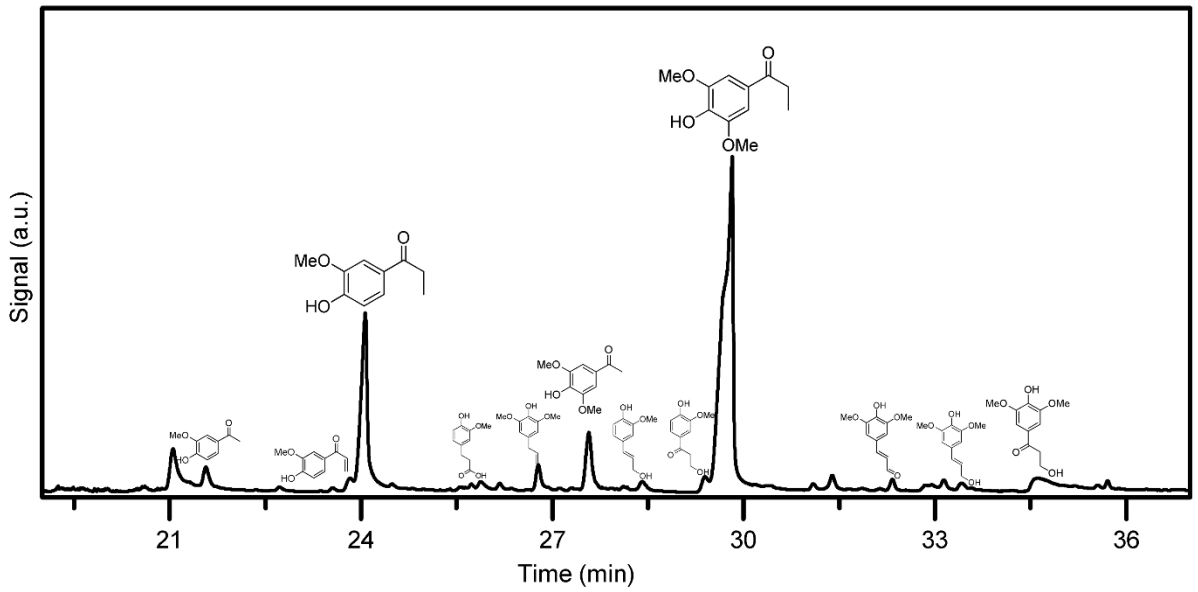

Supplementary Figure 6 | GC spectrum of product mixtures obtained from the photocatalytic conversion of native lignin in birch woodmeal.

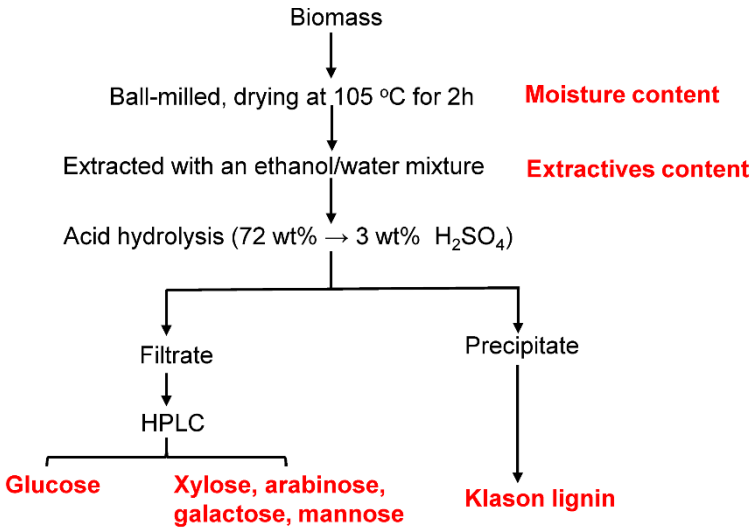

Supplementary Figure 7 | Procedures of compositional analyses.

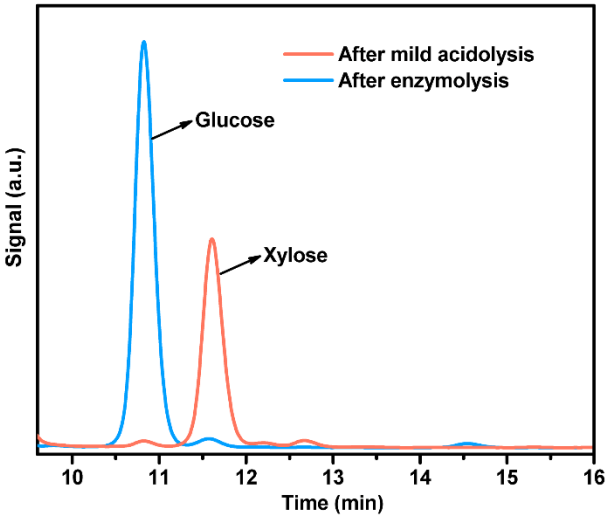

Supplementary Figure 8 | HPLC spectra of products obtained from the acidolysis and enzymolysis.

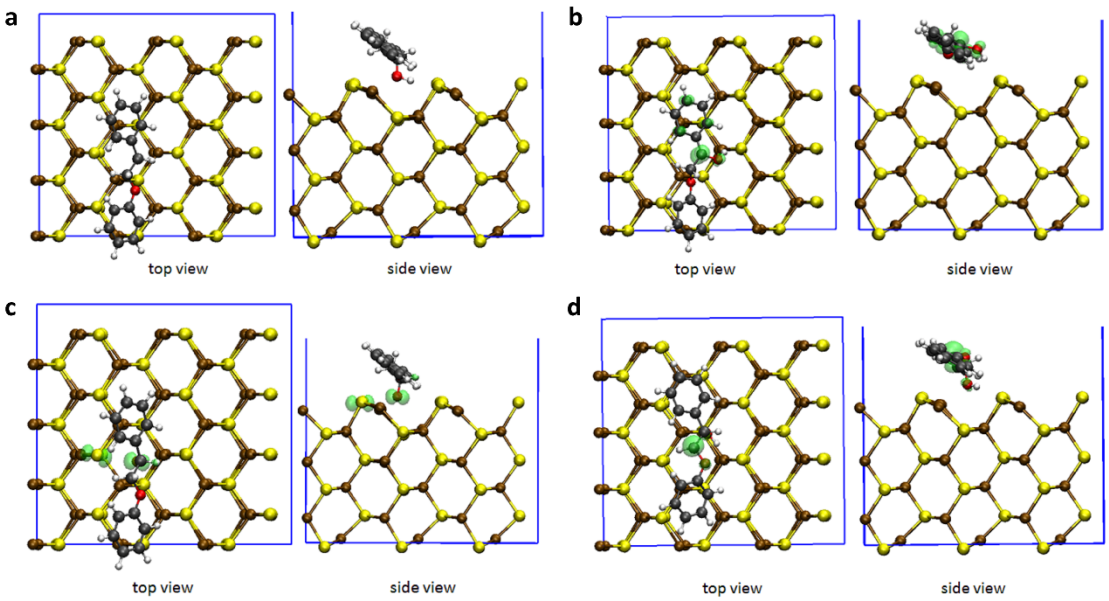

Supplementary Figure 9 | Computation models. Top views and side views of the adsorption states on CdS(110) surface. **a,** PP-ol. **b,** C_α radical intermediate. **c**, O radical intermediate. **d,** C_β radical intermediate. Cd, S, C, O and H atoms are represented in brown, yellow, grey, red and white, respectively. The spin density of the electronic hole is visualized by green isosurfaces with the density of 0.01.

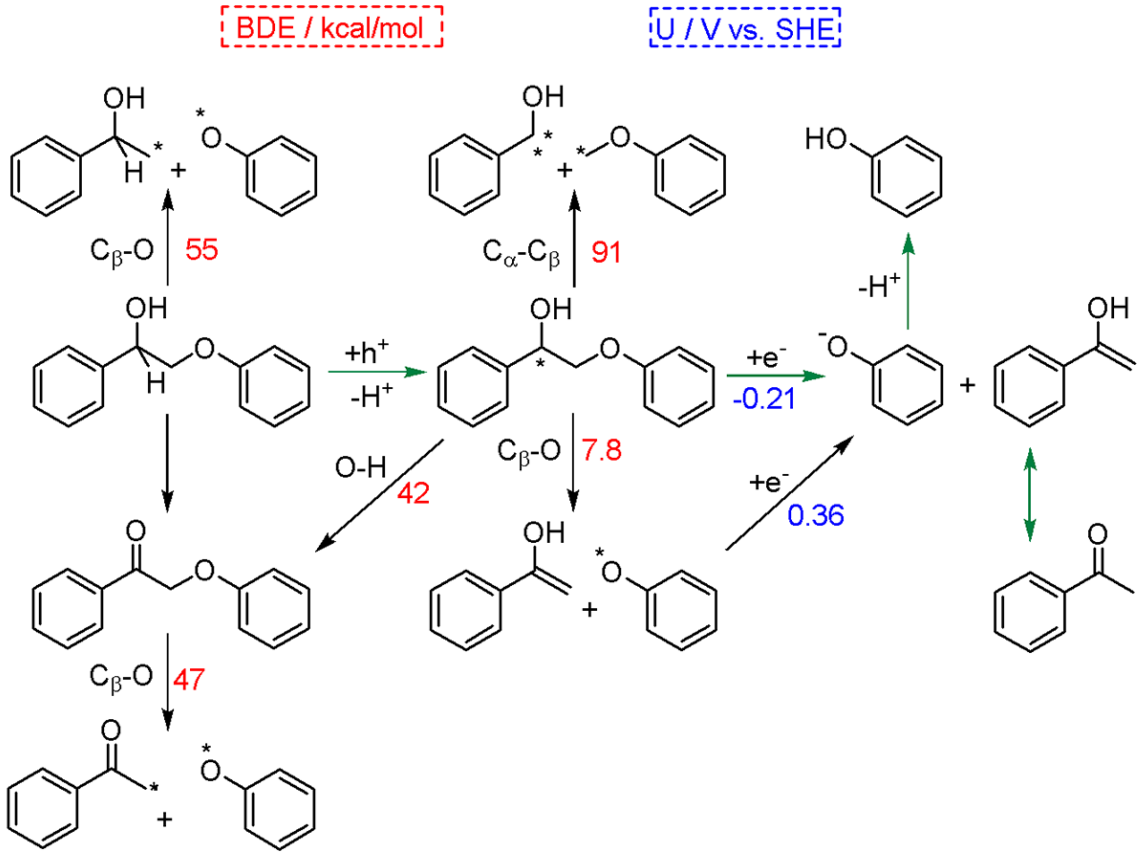

Supplementary Figure 10 | Bond dissociation energies (red) and redox potentials (blue) by using the B3LYP, CPCM solvent model.

Supplementary Table 1 | Comparison of performances between our photocatalytic system and some typical thermocatalytic systems for the conversion of PP-ol

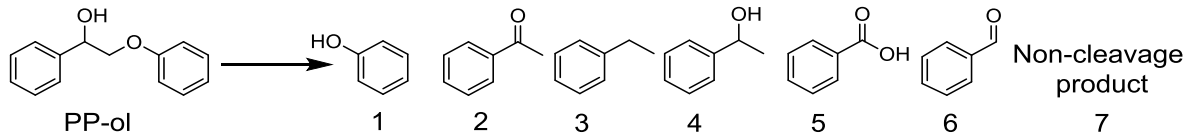

Catalyst	Reaction conditions	Conv. (%)	Yield (%)							
			1	2	3	4	5	6	7	Ref.
CdS NPs	0.1 MPa N_2, RT, visible light, 12 h	97	92	91						This work
CdS QD-4.4nm	0.1 MPa N_2, RT, visible light, 3 h	99	93	91						
Homogeneous catalytic systems										
$Cu(OAc)_2$-DMSO	80 ºC, 0.4 MPa O_2, 6 h, KOH	99					79			30
$Ru(H)_2(CO)(PPh_3)_3$ -ligand	135 ºC, 45 min	48	32	36					11	31
1. $VOSO_4$ 2. $Cu(OAc)_2$-ligand	1. TEMPO, 0.4 MPa O_2 , 100 ºC, 24 h 2. 0.4 MPa O_2, 80 ºC, 6 h	(76) 96	88				93			32
$Sc(OTf)_3$	200 ºC, 2h, Lewis acids	100	63							33
$(HQ)2V^v(O)(O^iPr)$	100 ºC, 48h	58	45				46		16	34
$VO(acac)_2$	0.1 MPa O_2, 80 ºC, 8 h	94	49				26	4.4		35
$[Fe(acac)_3$	140 ºC, 24 h, *t*BuONa, $LiAlH_4$	--	83			41				36
KO*t*Bu	180 ºC, 24 h, $LiAlH_4$	--			74					37
Heterogeneous catalytic systems										
NiMo sulfide	1.0 MPa H_2, 180 ºC, 1 h	69	8		6				36	38
HTC-as(NO_3)	275 ºC, 1 h	83	86	73						39
W_2C/AC	0.69 MPa H_2, 260 ºC, 2 h	100	71	44	15					40
$Pd_{50}Ag_{50}/Fe_3O_4$ /N-rGO	120 ºC, 3 h, HCOOH	100	99		98					41
Pd/CeO_2	0.1 MPa O_2, 185 ºC, 24 h	64	48	38					12	42
$Ni_{85}Ru_{15}$	10 bar H_2, 130 ºC, 1 h	100	0.3		9.3	7.6			>20	43
Cu/ γ-Al_2O_3	25 bar H_2, 150 ºC, 21 h	52	22		19					44
LCN	80 ºC, 24 h	88		1.2			24	0.2	38	45
$Ni_{70}Au_{30}$	1 MPa H_2, 130 ºC, PVP	99	38		4	27			12	46

Supplementary Table 2 | Control experiments with different solvents

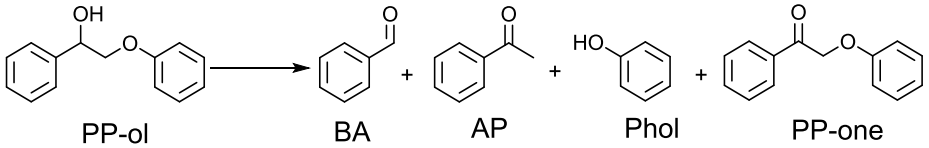

Solvent	Conversion (%)	Yield (%)		
		AP	Phol	PP-one
CH_3CN	99	91	93	1
CH_3OH	96	89	92	0
Cyclohexane	95	85	84	8
$CH_3OH:H_2O$=1:1	92	87	88	1

Reaction conditions: catalyst, CdS QD−4.4 nm, 10 mg; reactant (PP-ol), 20 mg (0.1 mmol); solvent, 5.0 mL; atmosphere, N_2; light source, Xe lamp (λ = 420-780 nm), 300 W; irradiation time, 3 h.

Supplementary Table 3 | Assignments of $^{13}C-^{1}H$ cross signals for quantification of different monomers and linkages in lignin

Label*	**δC/δH (ppm)**	**Assignments**
$S_{2,6}$	104.1/6.75	$C_{2,6}$-$H_{2,6}$ in syringyl units (S)
$S'_{2,6}$	106.9/7.31	$C_{2,6}$-$H_{2,6}$ in oxidized S units (S')
S condensed	106.6/6.43	C_x-H_x in condensed S
G_2	111.6/7.06	C_2-H_2 in guaiacyl units (G)
$PB_{2,6}$	130.9/7.64	$C_{2,6}$-$H_{2,6}$ in p-Hydroxybenzoate
p-$CE_{2,6}$	130.2/7.52	$C_{2,6}$-$H_{2,6}$ in p-coumarate (PCE)
$A_{\beta 1}$ (S/G-S)	87.0/4.26	C_β-H_β in β-O-4 unit
$A_{\beta 2}$ (S/G-G)	85.6/4.72	C_β-H_β in β-O-4 unit
B_α	87.5/5.45	C_α-H_α in phenylcoumaran (B)
C_α (2H)	85.1/4.72	C_α-H_α in β-β resinol (C)

*See Supplementary Fig. 4 for the structures of these labels.

Supplementary Table 4 | Integrated results of monomers and linkages in birch woodmeal based on the 2D HSQC NMR spectra

	Various monomers*						Linkages†			
	S	S'	S''	G	PB	*p*-CE	A_1	A_2	B	C
Birch	1	0.20	-	0.26	-	-	0.37	0.12	-	0.070

*See Supplementary Fig. 4 for the structures of S, S', G, PB, *p*-CE. S'' denotes S condensed. †See Supplementary Fig. 4 for the details of A, B and C.

Total C_9 units = (S/2) + (S'/2) + S condensed + G + (PB/2) + (p-CE/2)

Number of linkages per 100 C_9 units = linkage (A, B or C)/total C_9 units × 100

S/G = ((S+S')/2)/G = 2.3

P (β-O-4) = 57%

Theoretical maximum monomer yield (%) = 32%

Supplementary Table 5 | Lists of monomeric products from photocatalytic conversion of native lignin in birch woodmeal

Yield (wt%)	1	2	3	4	5	6	7	8	9	10	11	12
	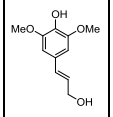				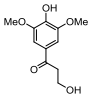			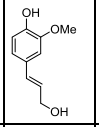	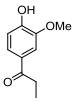	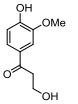	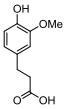	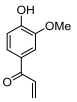
Birch	0.59	14	0.1	1.7	1.5	0.60	0.21	0.28	6.6	0.49	0.29	0.31
Birch*	0.95	12	0.2	2.7	1.5	0.63	0.48	0.63	4.9	0.95	0.13	0.41

* Scaling-up experiments performed with 300 mg birch woodmeal in a 50 mL quartz reactor after 16 h.

The products were grouped into categories of S-ketone, G-ketone and others. The yields of products in different categories were calculated using the following equations:

S ketone = 2 + 3 + 4 + 5

G ketone = 9 + 10 + 12

Others = 1 + 6 + 7 + 8 + 11

S/G = (1+2 + 3 + 4 + 5 + 6 + 7)/ (9 + 10 + 11 + 12)

Supplementary Table 6 | Photocatalytic conversion of native lignin in birch woodmeal using different catalysts as well as photocatalytic conversion of PP-ol using CdS-MPE

Yield (wt%) / Catalyst	1	2	3	4	5	6	7	8	9	10	11	12
	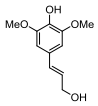		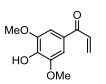	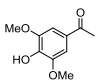	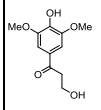		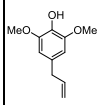	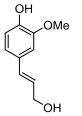	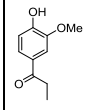	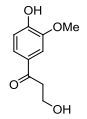	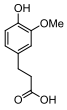	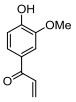
CdS-MPE	0.8	1.4	-	0.44	0.77	-	-	0.60	0.56	0.18	0.11	-
CdS-NP	0.14	0.06	-	0.08	0.13	-	0.22	-	0.17	0.17	-	0.23
$ZnIn_2S_4$	0.60	-	-	0.17	-	0.02	0.53	0.24	-	-	-	0.36

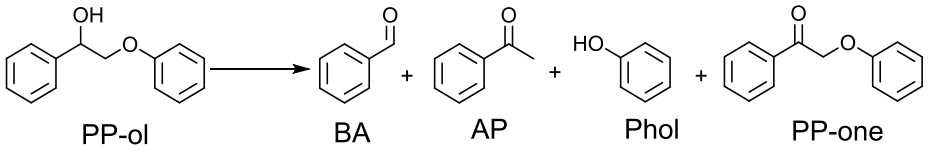

Catalyst	Conversion (%)	Yield (%)		
		AP	Phol	PP-one
CdS-MPE	99	88	89	5

Supplementary Table 7 | Compositions of birch woodmeal before and after photocatalytic conversion of native lignin

Substrate birch woodmeal	Moisture (wt%)	Extractives (wt%)	Weight fraction based on dried extracted biomass*† (wt%)					
			Glu	Xyl	Ara	Man	Gal	KL
Before reaction	8.7	3.2	44	20	0.48	0.51	0.31	19
After reaction	-	-	43	18	0.42	0.32	0.28	-

*"Glu" refers to glucose; "Xyl" refers to xylose; "Ara" refers to arabinose; "Gal" refers to galactose; "Man" refers to mannose; "KL" refers to Klason lignin. †The weight fraction after reaction was relative to the initial substrate weight.

Supplementary Table 8 | Retention time and effective carbon number (ECN) of major products

Compound number/ Ret. time/ ECN	**Compound structure**	**Compound number/ Ret. time/ ECN**	**Compound structure**	**Compound number/ Ret. time/ ECN**	**Compound structure**
1/ 33.2/ 7.65	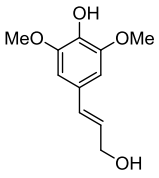	**2/ 29.8/ 7.25**	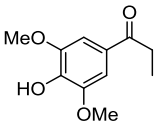	**3/ 29.9/ 8.15**	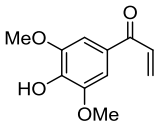
4/ 27.6/ 6.25	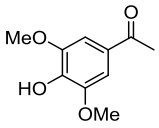	**5/ 34.7/ 6.6**	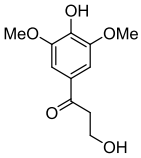	**6/ 32.4/ 7.25**	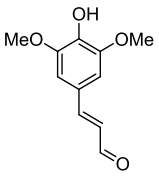
7/ 26.2/ 8.15	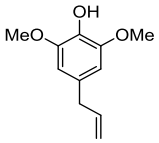	**8/ 28.4/ 7.65**	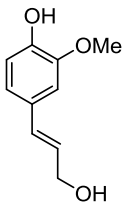	**9/ 24.1/ 7.25**	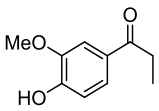
10/ 29.6/ 6.6	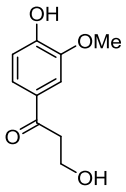	**11/ 25.9/ 7.25**	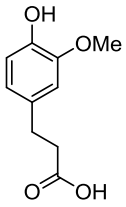	**12/ 24.2/ 7.25**	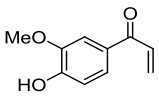

Supplementary Table 9 | Calculated dehydrogenation potential (in V) of PP-ol in vacuum and on CdS surfaces by using the PBE and the HSE06 functionals

PP-ol	$U_{dh}^{o}{}^{*}$ vs SHE (V)			
	PBE		HSE06	
	surface	vacuum	surface	vacuum
C_{α}−H	0.92	0.90	1.10	1.10
C_{β}−H	1.36	1.50	1.54	1.65
O−H	1.48	1.89	1.83	1.99

Supplementary References

1. Xiong, Y. *et al.* Growth and phase-transformation mechanisms of nanocrystalline CdS in Na_2S solution. *J. Phys. Chem. C* **112**, 9229-9233 (2008).
2. Yu, W. W. & Peng, X. Formation of high-quality CdS and other II–VI semiconductor nanocrystals in noncoordinating solvents: Tunable reactivity of monomers. *Angew. Chem. Int. Ed.* **41**, 2368-2371 (2002).
3. Chang, C. M., Orchard, K. L., Martindale, B. C. & Reisner, E. Ligand removal from CdS quantum dots for enhanced photocatalytic H_2 generation in pH neutral water. *J. Mater. Chem. A* **4**, 2856-2862 (2016).
4. Mansfield, S. D., Kim, H., Lu, F. & Ralph, J. Whole plant cell wall characterization using solution-state 2D NMR. *Nat. Protol.* **7**, 1579-1589 (2012)
5. Shuai, L. *et al*. Formaldehyde stabilization facilitates lignin monomer production during biomass depolymerization. *Science* **354**, 329-333 (2016)
6. Akinosho, H. *et al*. Effects of biomass accessibility and Klason lignin contents during consolidated bioprocessing in populus trichocarpa. *ACS Sustain. Chem. Eng.* **5**, 5075-5081 (2017)
7. VandeVondele, J. *et al.* Quickstep: Fast and accurate density functional calculations using a mixed Gaussian and plane waves approach. *Comput. Phys. Commun.* **167**, 103-128 (2005).
8. Lippert, G., Hutter, J. & Parrinello, M. A hybrid Gaussian and plane wave density functional scheme. *Mole. Phys.* **92**, 477-488 (1997).
9. VandeVondele, J. & Hutter, J. An efficient orbital transformation method for electronic structure calculations. *J. Chem. Phys.* **118**, 4365-4369 (2003).
10. Hartwigsen, C., Goedecker, S. & Hutter, J. Relativistic separable dual-space Gaussian pseudopotentials from H to Rn. *J. Chem. Phys.* **58**, 3641-3662 (1998).
11. VandeVondele, J. & Hutter, J. Gaussian basis sets for accurate calculations on molecular systems in gas and condensed phases. *J. Chem. Phys.* **127**, 114105 (2007).
12. Perdew, J. P., Burke, K. & Ernzerhof, M. Generalized gradient approximation made simple. *Phys. Rev. Lett.* **77**, 3865-3868 (1996).
13. Heyd, J., Scuseria, G. E. & Ernzerhof, M. Hybrid functionals based on a screened coulomb potential. *J. Chem. Phys.* **118**, 8207-8215 (2003).
14. Krukau, A. V., Vydrov, O. A., Izmaylov, A. F. & Scuseria, G. E. Influence of the exchange screening parameter on the performance of screened hybrid functionals. *J. Chem. Phys.* **125**, 224106 (2006).
15. Grimme, S., Antony, J., Ehrlich, S. & Krieg, H. A consistent and accurate ab initio parametrization of density functional dispersion correction (DFT-D) for the 94 elements H-Pu. *J. Chem. Phys.* **132**, 154104 (2010).
16. Cheng, J., Sulpizi, M., VandeVondele, J. & Sprik, M. Hole localization and thermochemistry of oxidative dehydrogenation of aqueous rutile TiO_2 (110). *ChemCatChem* **4**, 636-640 (2012).
17. Guidon, M., Hutter, J. & VandeVondele, J. Auxiliary density matrix methods for Hartree−Fock exchange

clculations. *J. Chem. Theory. Comput.* **6**, 2348-2364 (2010).

18. Guidon, M., Hutter, J. & VandeVondele, J. Robust periodic Hartree−Fock exchange for large-scale simulations using Gaussian basis sets. *J. Chem. Theory. Comput.* **5**, 3010-3021 (2009).
19. Guidon, M., Schiffmann, F., Hutter, J. & VandeVondele, J. Ab initio molecular dynamics using hybrid density functionals. *J. Chem. Phys.* **128**, 214104 (2008).
20. Cheng, J., Liu, X., VandeVondele, J., Sulpizi, M. & Sprik, M. Redox potentials and acidity constants from density functional theory based molecular dynamics. *Acc. Chem. Res.* **47**, 3522-3529 (2014).
21. Cheng, J., Liu, X., Kattirtzi, J. A., VandeVondele, J. & Sprik, M. Aligning electronic and protonic energy levels of proton-coupled electron transfer in water oxidation on aqueous TiO_2. *Angew. Chem. Int. Ed.* **53**, 12046-12050 (2014).
22. Frisch, M. J. *et al*. Gaussian 09 Revision D.01 (Gaussian Inc. Wallingford CT, 2009).
23. Becke, A. D. Density-functional exchange-energy approximation with correct asymptotic behavior. *Phys. Rev. A* **38**, 3098-3100 (1988).
24. Lee, C., Yang, W. & Parr, R. G. Development of the colle-salvetti correlation-energy formula into a functional of the electron density. *J. Chem. Phys.* **37**, 785-789 (1988).
25. Becke, A. D. Density-functional thermochemistry. 3. The role of exact exchange. J. Chem. Phys. **98**, 5648–5652 (1993).
26. Dunning Jr, T. H. Gaussian basis sets for use in correlated molecular calculations. I. The atoms boron through neon and hydrogen. *J. Chem. Phys.* **90**, 1007-1023 (1989).
27. Keith, J. A. & Carter, E. A. Theoretical insights into pyridinium-based photoelectrocatalytic reduction of CO_2. *J. Am. Chem. Soc.* **134**, 7580-7583 (2012).
28. Cossi, M., Rega, N., Scalmani, G. & Barone, V. Energies, structures, and electronic properties of molecules in solution with the C-PCM solvation model. *J. Comput. Chem.* **24**, 669-681 (2003).
29. Gagliardi, L. G., Castells, C. B., Rafols, C., Rosés, M. & Bosch, E. Static dielectric constants of acetonitrile/water mixtures at different temperatures and Debye−Hückel A and a_0B parameters for activity coefficients. *J. Chem. Eng. Data* **52**, 1103-1107 (2007).
30. Wang, M., *et al.*, Oxidative C(OH)-C bond cleavage of secondary alcohols to acids over a copper catalyst with molecular oxygen as the oxidant. *J. Catal.* **348**, 160-167 (2017).
31. Shaw, L., *et al.* Electronic and bite angle effects in catalytic C–O bond cleavage of a lignin model compound using ruthenium Xantphos complexes. *Catal. Sci. Technol.* **7**, 619-626 (2017).
32. Wang, M., *et al.* Two-step, catalytic C–C bond oxidative cleavage process converts lignin models and extracts to aromatic acids. *ACS Catal.* **6**, 6086-6090 (2016).
33. Jastrzebski, R., *et al.* Tandem catalytic depolymerization of lignin by water-tolerant Lewis acids and rhodium complexes. *ChemSusChem* **9**, 2074-2079 (2016).
34. Díaz-Urrutia, C., Sedai, B., Leckett, K. C., Baker, R. T. & Hanson, S. K. Aerobic oxidation of 2-

phenoxyethanol lignin model compounds using vanadium and copper catalysts. *ACS Sustainable Chem. Eng.* **4**, 6244-6251 (2016).

35. Ma, Y., Du, Z., Liu, J., Xia, F. & Xu, J. Selective oxidative C–C bond cleavage of a lignin model compound in the presence of acetic acid with a vanadium catalyst. *Green Chem.* **17**, 4968-4973 (2015)
36. Ren, Y., Yan, M., Wang, J., Zhang, Z. C. & Yao, K. Selective reductive cleavage of inert aryl C-O bonds by an iron catalyst. *Angew. Chem. Int. Ed.* **52**, 12674-12678 (2013).
37. Xu, H., *et al.* Reductive cleavage of inert aryl C–O bonds to produce arenes. *Chem. Commun.* **51**, 12212-12215 (2015).
38. Zhang, C., *et al.* Cleavage of the lignin β-O-4 ether bond via a dehydroxylation–hydrogenation strategy over a NiMo sulfide catalyst. *Green Chem.* **18**, 6545-6555 (2016).
39. Kruger, J. S., *et al.* Lignin depolymerization with nitrate-intercalated hydrotalcite catalysts. *ACS Catal.* **6**, 1316-1328 (2016).
40. Guo, H., *et al.* Tungsten carbide: A remarkably efficient catalyst for the selective cleavage of lignin C−O bonds. *ChemSusChem* **9**, 3220-3229 (2016).
41. Singh, A. K., *et al.* One-pot defunctionalization of lignin-derived compounds by dual-functional $Pd_{50}Ag_{50}/Fe_3O_4$/N-rGO catalyst. *ACS Catal.* **5**, 6964-6972 (2015).
42. Deng, W., *et al.* Oxidative conversion of lignin and lignin model compounds catalyzed by CeO_2-supported Pd nanoparticles. *Green Chem.* **17**, 5009-5018 (2015).
43. Zhang, J., *et al.*, A series of NiM (M= Ru, Rh, and Pd) bimetallic catalysts for effective lignin hydrogenolysis in water. *ACS Catal.* **4**, 1574-1583 (2014).
44. Strassberger, Z., Alberts, A. H., Louwerse, M. J., Tanase, S. & Rothenberg, G. Catalytic cleavage of lignin β-O-4 link mimics using copper on alumina and magnesia-alumina. *Green Chem.* **15**, 768-774 (2013).
45. Gao, Y., Zhang, J., Chen, X., Ma, D. & Yan, N. A metal-free, carbon-based catalytic system for the oxidation of lignin model compounds and lignin. *ChemPlusChem* **79**, 825-834 (2014).
46. Zhang, J., *et al.* Highly efficient, NiAu-catalyzed hydrogenolysis of lignin into phenolic chemicals. *Green Chem.* **16**, 2432-2437 (2014).